Nanoscale

ROYAL SOCIETY OF CHEMISTRY

PAPER

View Article Online
View Journal | View Issue

Cite this: *Nanoscale*, 2025, **17**, 20107

α-Ketoglutaric acid-derived carbon nanodots doped with manganese as fluorescent and MRI contrast agents

Ioana-Andreea Turin-Moleavin,†[a] Adina Coroaba, †[a] Adrian Fifere,*[a] Narcisa Laura Marangoci,[a] Mariana Pinteala, [a] Cristina Mariana Uritu, [a,b] Silviu Iulian Filipiuc, [a,b] Marius Dobromir,[c] Ionut Radu Tigoianu[d] and Tudor Pinteala[a,e]

Carbon nanodots (CNDs) are a class of nanomaterials under 10 nm known for their distinctive optical properties. In this work, we introduce α-ketoglutaric acid (KGA) as a novel carbon precursor for the hydrothermal synthesis of CNDs (KGA-CNDs), yielding particles with an average size of 1.9 nm. KGA's efficient manganese-binding capability facilitated the successful doping of CNDs (KGAMn-CNDs), resulting in a manganese content of 6%. The significant incorporation of transition metal points out the potential applications of manganese-doped carbon nanodots (CNDs) in magnetic resonance imaging (MRI). At a magnetic field strength of 1 Tesla, the longitudinal (r_1) and transverse (r_2) relaxivity values were 5.46 s^{-1} mM^{-1} and 46.83 s^{-1} mM^{-1}, respectively, surpassing the commercial Gd-based agent Gadoterate at 0.5 Tesla (r_1 = 3.58 s^{-1} mM^{-1}; r_2 = 21.6 s^{-1} mM^{-1}). The ratio of transverse to longitudinal relaxivity indicates the potential of KGAMn-CNDs for T_2-weighted contrast in MRI at clinically relevant magnetic field strengths. Fluorescence imaging demonstrated that both types of CNDs displayed strong fluorescence and high photostability, thereby confirming their potential as fluorescent probes. KGAMn-CNDs exhibited dual functionality, serving as contrast agents for fluorescence and MRI. These findings highlight the potential of KGA-derived CNDs as efficient dual-mode imaging agents and establish KGA as a versatile and innovative precursor for the development of CNDs with tunable physicochemical properties.

Received 1st August 2025,
Accepted 13th August 2025

DOI: 10.1039/d5nr03268g

rsc.li/nanoscale

Introduction

Carbon nanodots (CNDs) have emerged as promising fluorescent nanomaterials, particularly for biomedical applications where they offer advantages over conventional fluorophores or quantum dots.[1] Fluorescent molecules and quantum dots have long been used in fluorescence imaging to enable real-time visualization of physiological processes, providing valuable diagnostic information. However, molecular fluorophores often require complex synthetic routes and present limitations in functionalization, while quantum dots raise significant toxicity concerns due to their heavy metal content, constraining their clinical applicability. In contrast, CNDs combine facile synthesis with abundant surface functional groups, favourable optical properties, and high biocompatibility. CNDs exhibit attributes that make them suitable for bioimaging and associated biomedical applications. As a result, a wide variety of synthetic methods have been investigated in recent years, using both synthetic and natural compounds as precursors.[2–5]

Among imaging modalities, magnetic resonance imaging (MRI) is particularly valuable, providing high-resolution anatomical and functional information from deep tissues without the risks associated with ionizing radiation. Most clinically used MRI contrast agents are based on lanthanide ions, such as gadolinium (Gd^{3+}) and dysprosium, or transition metals like manganese (Mn^{2+}) and iron (Fe^{3+}).[6] Gadolinium-based complexes, particularly Gd-DTPA, remain the most widely employed; however, increasing evidence has linked Gd^{3+} exposure to nephrogenic systemic fibrosis,[7] encouraging the search for safer alternatives. Within the transition metal class,

[a]*Centre of Advanced Research in Bionanoconjugates and Biopolymers, "Petru Poni" Institute of Macromolecular Chemistry, 700487 Iasi, Romania.*
E-mail: fifere@icmpp.ro
[b]*Advanced Center for Research and Development in Experimental Medicine "Prof. Ostin C. Mungiu", "Grigore T. Popa" University of Medicine and Pharmacy, 700454 Iasi, Romania*
[c]*Research Centre on Advanced Materials and Technologies, Department of Exact and Natural Sciences, Institute of Interdisciplinary Research, "Alexandru Ioan Cuza" University of Iasi, Faculty of Physics, 700506 Iasi, Romania*
[d]*Physical Chemistry of Polymers, "Petru Poni" Institute of Macromolecular Chemistry, 700487 Iasi, Romania*
[e]*Department of Orthopedics and Traumatology, Faculty of Medicine, "Grigore T. Popa" University of Medicine and Pharmacy, 700115 Iasi, Romania*
†These authors contributed equally to this work.

manganese has emerged as a promising candidate due to its high-spin electronic configuration, favourable relaxivity profile, and superior biocompatibility.[6,8] To integrate fluorescence imaging with MRI in a single diagnostic platform, metal-doped CNDs have been developed in recent years, with manganese doping receiving particular attention.[9,10] Although many studies on manganese-doped CNDs do not precisely quantify metal content, some general trends are apparent. Manganese doping levels between 0.1 and 2% are commonly reported,[10,11] while concentrations in the range of 2 to 4% appear even more frequently.[12–14] Higher doping levels of 5 to 10% are relatively rare.[15,16] In general, the MRI contrast performance of manganese-doped CNDs tends to improve with increased manganese content. Nonetheless, effective contrast enhancement has also been demonstrated at moderate doping levels of up to 2%.[17]

α-Ketoglutaric acid (KGA) represents a promising, yet unexplored precursor for synthesizing CNDs from compounds containing only carbon and oxygen. It is a key intermediate in the Krebs cycle, which plays an essential role in cellular metabolism.[18] Its established use as an adjuvant in pharmaceuticals and dietary supplements[19] further highlights the relevance of developing new KGA-derived nanomaterials. In this work, KGA was investigated for the first time as a precursor for the synthesis of CNDs. Since KGA does not contain heteroatoms like nitrogen or sulfur, the initial efforts focused on producing and characterizing undoped CNDs without introducing additional heteroatom sources. At the same time, the possibility of doping these CNDs with manganese was examined, with the goal of developing effective MRI contrast agents. Accordingly, the work presents the hydrothermal synthesis and thorough characterization of CNDs prepared solely from KGA. The molecule's two carboxyl groups and an α-position ketone are anticipated to coordinate Mn^{2+} ions prior to carbonization, thus facilitating the formation of manganese-doped CNDs during the hydrothermal process.

The synthesized CNDs showed quantum yields (QY) up to 20% for KGA-CNDs and 16% for KGAMn-CNDs (relatively high values for CNDs lacking nitrogen or sulphur heteroatoms) supporting their suitability for biomedical use.[20,21] Fluorescence imaging confirmed a linear correlation between fluorescence intensity and CND concentration, indicating good contrast. The fluorescence intensity showed a minimal decrease after ten consecutive scans, indicating a high degree of photostability. This characteristic is important for imaging applications necessitating multiple scans over prolonged durations. Additionally, the manganese content in KGAMn-CNDs reaches approximately 6%, demonstrating that KGA is an effective precursor for the efficient incorporation of Mn^{2+} into CNDs. This highlights its potential for producing CNDs intended as contrast agents in MRI. Relaxometric analysis demonstrated that the longitudinal (r_1) and transverse (r_2) relaxivities of the KGAMn-CNDs sample are 5.46 and 46.83 s^{-1} mM^{-1}, respectively. The r_1 relaxivity is comparable to that of commercially available gadolinium-based contrast agents, including Gadovist, Magnevist, Omniscan, and ProHance.[22] The r_2/r_1 ratio indicated that KGAMn-CNDs predominantly exhibit T_2 relaxation behaviour, with r_2 relaxivity exceeding that of the commercial gadolinium-based agent, Gadoterate.[23] The notable T_1 relaxation combined with significant T_2 relaxation highlights the potential of KGAMn-CNDs as an MRI contrast agent, especially for improving T_2-weighted contrast at clinically relevant magnetic field strengths.

These findings indicate the potential of KGA-derived CNDs for dual-mode bioimaging, effectively integrating fluorescence and MRI for applications relevant to routine health monitoring. Furthermore, this work may establish a basis for the development of new CND systems or exploring alternative doping strategies with manganese or other paramagnetic transition metals.

Materials and methods

Chemicals

KGA (99%), manganese(II) chloride tetrahydrate (99.99% trace metals basis), sodium chloride (≥99%, ACS reagent), and bovine serum albumin (BSA, lyophilized powder, ≥96%) were purchased from Sigma-Aldrich (Germany). Phosphate-buffered saline (PBS) solutions with pH values of 3, 5, 6, 7, 8, 9, 10, 11, 12, and 13 were obtained from Honeywell, Fluka (Germany).

Preparation of KGA-CNDs and KGAMn-CNDs

KGA-CNDs were synthesized using a hydrothermal process with KGA as the sole carbon source. Specifically, 1.46 g of KGA (10 mmol) was dissolved in 10 mL of deionized water and transferred to a 20 mL Teflon-lined autoclave. The autoclave was heated at 200 °C for 6 hours. For the preparation of manganese-doped CNDs (KGAMn-CNDs), 0.197 g of manganese(III) chloride tetrahydrate ($MnCl_2{\cdot}4H_2O$, 1 mmol) was added to the KGA solution prior to heating. After the reaction, autoclaves were allowed to cool naturally over at least 10 hours to minimize effervescence and prevent loss of the product. The resulting yellow solutions were centrifuged at 5000 rpm for 20 minutes, and the supernatant was filtered through a 0.2 μm filter to remove larger residues. The filtered solutions were then purified by dialysis against deionized water using a 1 kDa cut-off membrane (Spectra/Por®, Repligen) for 72 hours. The purified solutions were stored at room temperature in the dark, remaining clear and free of turbidity for at least three weeks.

Physical characterization techniques

The Attenuated Total Reflectance Fourier Transform Infrared Spectroscopy (ATR FT-IR) spectra were acquired using a Shimadzu IRTracer-100 Fourier Transform Infrared Spectrophotometer equipped with a PIKE Technologies GladiATR single-reflection ATR module. Data were processed with Shimadzu's LabSolutions IR software and graphically refined in OriginPro 2020b.

Morphological and dimensional analysis of CNDs was performed on a Hitachi High-Tech HT7700 transmission electron

microscope (TEM), operating in high contrast mode at an accelerating voltage of 120 kV. The samples were deposited undiluted in 10 μL volumes onto 400 Mesh carbon-coated copper grids (TED PELLA). ImageJ 1.48r software was used for image processing.[24]

The Ultraviolet–Visible (UV-Vis) spectra were recorded using a PerkinElmer Lambda 25 UV-Vis spectrophotometer with quartz cuvettes having a 10 mm optical path. Deionized water was used as the blank, and the spectra were collected in double-beam mode.

Electron spin resonance (ESR) analysis was performed using a Bruker EMX X-band EPR spectrometer (9.8 GHz, 100 kHz modulation). Spectra were recorded at room temperature (22 °C) under the following conditions: center field 3462 G, receiver gain 40 dB, modulation amplitude 3 G, attenuation 10 dB (20 mW), and time constant 40.96 ms. Samples were injected into quartz capillary tubes (100 μL volume, 1 mm internal diameter, 125 mm length). $MnCl_2{\cdot}4H_2O$ solutions (0.015–6 mg mL^{-1}) were used for calibration, and the intensity of the third Mn^{2+} ESR peak (marked "*" in Fig. S1) was used to generate the calibration curve.

Transient absorption (TA) maps were recorded on an Edinburgh FLS980 photoluminescence spectrometer for both KGA-CNDs and KGAMn-CNDs aqueous dispersions, using Nd YAG Laser, maxim output 500 mJ, pulse duration 4–6 ns at excitation wavelength 355 nm. All experiments were conducted at room temperature in quartz cuvettes with a 10 mm path length.

Steady-state fluorescence spectra were collected using a Horiba Scientific FluoroMax-4 fluorometer over an excitation range of 300–530 nm in 1 cm path length cuvettes. Absolute quantum yields (QY) and excited-states lifetimes were measured on the same instrument equiped with a Quanta-Φ integration sphere and a FluoroHub Time-Correlated Single-Photon Counting (TCSPC) module. Excitation was provided by 370 nm and 455 nm LED sources. Experimental lifetime decays were fitted to a multi-exponential decay model, as detailed in the SI.

X-ray photoelectron spectroscopy (XPS) was carried out using a ULVAC-PHI 5000 VersaProbe spectrometer equipped with an Al Kα radiation source (1486.7 eV), operated at 20 mA and 15 kV. High-resolution spectra (58.7 eV pass energy, 0.1 eV step) were processed with CasaXPS software (version 2.3.26PR1.0), using the C 1s peak of adventitious carbon at 285.0 eV as an internal calibration reference.

The X-ray diffraction (XRD) patterns of the samples were measured with a Rigaku SmartLab X-ray diffractometer in Bragg–Bretano geometry using a Cu anode (X-ray wavelength of 1.5406 Å), in the angular range 5–90° (2θ), with a scanning step of 0.02° and a recording rate of 3° min^{-1}.

Energy-dispersive X-ray spectroscopy (EDX) elemental mapping was performed on a Thermo Scientific Verios G4 UC Scanning electron microscope equipped with Energy Dispersive X-ray spectroscopy analyzer (Octane Elect Super SDD detector). For this investigation the samples were fixed on aluminum stubs with double-adhesive carbon tape. EDX mapping was performed using an acceleration voltage of 20 kV and a spot size of 6.4 nA.

The zeta potential measurements were carried out on a Malvern Panalytical ProRED Particle Size Analyzer using DTS1070 disposable folded capillary cells. Data were analyzed with ZS XPLORER Software v3.3.0.42.

The pH influence on photoluminescence (PL) intensity was assessed using 0.5 mg mL^{-1} CND solutions prepared in PBS at pH of 3, 5, 6, 7, 8, 9, 10, 11, 12, and 13. After 30 min equilibration at room temperature, PL spectra were recorded (λ_{exc} = 420 nm). The influence of manganese, sodium chloride, and BSA on PL intensity was investigated using a similar experimental approach. Stock aqueous solutions were prepared with the following concentrations: 12 mg mL^{-1} KGA-CND, 9 mg mL^{-1} KGAMn-CND, 260 mg mL^{-1} $MnCl_2{\cdot}4H_2O$, 15 mg mL^{-1} NaCl, and 12 mg mL^{-1} BSA. Experimental samples were prepared by mixing appropriate volumes of these solutions to ensure a constant concentration of 0.5 mg mL^{-1} for KGA-CND or KGAMn-CND in all cases. For the analysis of NaCl and BSA effects, their concentrations were varied as follows: 0.1, 0.5, 1, 2, 5, and 10 mg mL^{-1}. To investigate the effect of Mn^{2+} ions, solutions of $MnCl_2{\cdot}4H_2O$ were prepared at concentrations ranging from 1 to 10 mg mL^{-1} (corresponding to 5 to 50 mM of Mn^{2+}). For the BSA experiments, the fluorescence intensity of a BSA-only control was measured to exclude any intrinsic fluorescence from the protein. The Mn^{2+} and NaCl tests were carried out in deionized water, while BSA experiments were performed in PBS. All solutions were allowed to equilibrate at room temperature for 30 minutes before measurements. PL spectra were recorded using an excitation wavelength of 420 nm. Each measurement was performed in triplicate, and the arithmetic mean of the recorded values was reported.

Fluorescence imaging

Fluorescence imaging of KGA-CNDs and KGAMn-CNDs was performed using a Spectral Instruments Imaging AMI HTX system, capable of acquiring fluorescence, bioluminescence, and X-ray images of small animals and cell culture plates. The system supports detection and quantification of optical signals across 10 selectable excitation wavelengths (430–745 nm) and 10 emission wavelengths (530–790 nm). Image analysis was carried out with Aura software (v4.5.0) for quantitative processing.

To evaluate the fluorescence imaging agent capacity of the compounds, eight serial concentrations (0.33, 0.83, 1.67, 2.5, 3.33, 5, 6.67, and 10 mg mL^{-1}) of KGA-CNDs and KGAMn-CNDs were prepared in water and pipetted (300 μL per well) into a 96-well black assay plate (non-fluorescent). All samples were scanned under identical conditions: λ_{ex} = 430 nm, λ_{em} = 530 nm, PE = 5%, Exp = 1 s, FSTOP = 2. Photostability was evaluated by measuring fluorescence intensity after 10 consecutive scans under the same acquisition settings. Quantification of fluorescence for each concentration was performed by defining uniform regions of interest (ROI) for each well, with Aura software automatically reporting the total photon emission rate (photons per sec) for each ROI.

MR imaging

The manganese content in KGAMn-CNDs enables their potential application as MRI contrast agents, which was assessed following established methodologies.[25–27] The experimental design focused on evaluating MRI signal enhancement in both T_1- and T_2-weighted sequences using a series of KGAMn-CND concentrations embedded in 1% agarose gel prepared with 0.01 M phosphate buffer at pH 7.4. Agarose gel is widely used in phantom MRI experiments because its concentration can be adjusted to accurately mimic the properties of various soft tissues.[28]

Starting from a stock solution of KGAMn-CNDs at 10 mg mL^{-1} (corresponding to 0.6 mg mL^{-1} Mn^{2+} or 10.91 mM), seven manganese concentrations (0.027, 0.055, 0.082, 0.11, 0.16, 0.22, and 0.33 mM) were prepared by serial dilution in the agarose gel. Aliquots of 3 mL for each concentration were placed in wells of a cell culture plate and imaged using a 1 Tesla small-animal MRI scanner (Mediso nanoScan PET-MRI) employing both T_1 and T_2 imaging protocols. MRI performance was characterized by measuring spin–lattice (T_1) and spin–spin (T_2) relaxation times to determine the compound's efficacy in shortening relaxation times and thus enhancing contrast. T_1 relaxation times were measured using gradient echo (T_1-GRE) sequences, while T_2 relaxation was evaluated *via* fast spin echo (T_2-FSE) sequences.

The two-point estimation method was used to calculate the T_1 relaxation times, according to eqn (1):

$$\ln\left[\frac{(I_1 \sin\theta_2 - I_2 \sin\theta_1)}{(I_1 \sin\theta_2 \cos\theta_1 - I_1 \sin\theta_2 \cos\theta_1)}\right] = \frac{-\mathrm{TR}}{T_1} \quad (1)$$

where: I_1, I_2 – the mean signal intensities measured inside the ROI drawn in the centre of the samples at 10 and 60° flip angles; TR – repetition time; θ_1 and θ_2 – the flip angles.

The most relevant acquisition parameters for T_1 measurements were: TR = 358 ms, TE = 3.8 ms (the echo time), NSA = 2 (the number of excitations), slice thickness = 3 mm, gap = 1 mm and a variable flip angle FA = 10, 20, 60 and 70°. The circular ROI with a 10 mm diameter was positioned in the central area of each sample, and the software automatically generated mean signal intensity values for further analysis.

For the T_2 relaxation time determination, the working parameters were: TR = 1896 ms, NSA = 2, slice thickness = 3 mm, gap = 1 mm, and a variable echo time TE = 20, 40, 80, 120 ms. The data were extracted similarly as for T_1, using identical ROIs (10 mm diameter). The T_2 values for each sample were calculated from the ^{1}H relaxometry tool of the Nucline software of the equipment based on eqn (2):

$$I = A \cdot \exp\left(\frac{\mathrm{TE}}{T_2}\right) \quad (2)$$

where: I – signal intensity in the region of interest (ROI), A – initial intensity of the signal, TE – echo time, T_2 – transverse relaxation time.

Cell viability assay

The biocompatibility of KGA-CNDs and KGAMn-CNDs was assesed using the CellTiter-Glo® 2.0 Assay (Promega, Madison, WI USA), according to the manufacturer's instructions. Human gingival fibroblasts (HGF, CLS Cell Lines Service GmbH, Eppelheim, Germany) were cultured in αMEM medium supplemented with 10% fetal bovine serum and 1% antibiotic-antimycotic (all from Gibco, Thermo Fisher Scientific, Waltham, MA, USA). Cells were seeded in 96-well white opaque tissue culture-treated plates at a density of 50 000 cells per mL and allowed to adhere overnight. The following day, cells were incubated in triplicate experiments with different concentrations of CNDs (10, 25, 50, 75, 100 μg mL^{-1}) for 24 h. For cell viability determination, CellTiter-Glo® reagent was added, and luminescence was recorded using a BMG LABTECH FLUOstar® Omega microplate reader. Treated cells' viability was calculated as percentage of untreated cells' viability and data were represented graphically as means ± standard deviations.

Results and discussion

Synthesis of CNDs

KGA was chosen as the precursor for CND synthesis due to its molecular structure, which includes two carboxylic groups and one ketone group (Fig. 1). The functional groups present in KGA promote polymerization, leading to the formation of nanoparticles with branched polymer structures before carbonization.[29] Additionally, the vicinal carboxyl and ketone groups suggest that KGA can act as a chelating agent, facilitating complexation with transition metals such as manganese.[30]

KGA-CNDs were synthesized by hydrothermal method, as illustrated in Fig. 1. An aqueous solution containing 10 millimoles of KGA was heated to 200 °C in a 20 ml Teflon-lined autoclave for a duration of 6 hours. For the synthesis of KGAMn-CNDs, divalent manganese ions were incorporated into the KGA precursor solution by adding manganese chloride ($MnCl_2$) at a molar ratio of 10 : 1 (KGA to $MnCl_2$). Initially, the solutions were transparent; however, following hydrothermal treatment, they turned dark brown. The solutions were purified through centrifugation and filtration, followed by dialysis with membranes having a cut-off of 1 kDa, as detailed in the experimental section and illustrated in Fig. 1.

Numerous synthesis protocols suggest a dialysis duration ranging from 24 to 48 hours.[31,32] In the present study, the

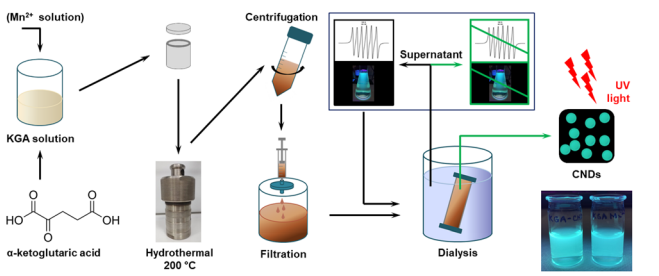

Fig. 1 Schematic illustration of the synthesis and purification procedures for CNDs.

optimal dialysis time was empirically determined by periodically extracting aliquots of the supernatant from the dialysis vessel and visually assessing their fluorescence under UV irradiation with a laboratory UV lamp (Fig. 1). This method allowed monitoring of fluorescent by-product removal. After 72 hours, no fluorescence was detectable, even when the dialysis water was concentrated by evaporation, indicating effective elimination of fluorescent impurities.

The removal of unbound manganese ions in KGAMn-CNDs was assessed by ESR analysis of aliquots collected from the dialysis water (Fig. S1). Manganese ions were detectable up to 30 hours of dialysis, after which they were no longer observed (even following concentration of the dialysis water by evaporation). This indicates that free Mn^{2+} ions were successfully removed from the dispersion through the dialysis process.

It is worth noting that the appropriate purification strategy for CNDs remains a subject of on-going discussion, with protocols often tailored to specific applications. Nevertheless, a combination of centrifugation, filtration and dialysis remains the most commonly adopted approach for CNDs purification.

The zeta potential values of CNDs were −12 mV for KGA-CNDs and −7.8 mV for KGAMn-CNDs (Fig. S2), suggesting the presence of surface carboxyl and hydroxyl functional groups. The reduced negative zeta potential observed for the manganese-doped CNDs is associated with the presence of divalent Mn^{2+} ions on the CNDs surface. Such negative zeta potential values ensure colloidal stability and are commonly observed in CNDs synthesized through hydrothermal methods at high temperatures (~200 °C),[33,34] where the thermal decomposition of surface functional groups can also contribute to the overall surface charge characteristics.

Physicochemical characterization of KGA-CNDs and KGAMn-CNDs

ATR FT-IR study of KGA-CNDs and KGAMn-CNDs. The FT-IR spectrum of the KGA (Fig. 2, black graph) displays the characteristic vibrational features of the precursor, with several well-defined absorption bands. Vibrations observed in the 680–872 cm^{-1} range correspond to C–H bending and ketone skeletal vibrations from the $-COO^-$ group.[35,36] The sharp bands observed in the 1225–1320 cm^{-1} region can be assigned to C–O stretching vibrations, while those in the 1400–1450 cm^{-1} region correspond to O=C–OH and O–H bending vibrations from carboxylic groups.[35,37] A strong band at 1690–1704 cm^{-1} originates from carbonyl (C=O) stretching of aldehyde and carboxyl functionalities.

The FT-IR spectra of KGA-CNDs and KGAMn-CNDs (Fig. 2, red and blue) share similar overall profiles, yet differ distinctly in band shape and position relative to the precursor. The disappearance of several characteristic KGA bands alongside the appearance of broad new absorptions in regions typical for unsaturated chemical groups confirms successful conversion into CNDs. Notably, new bands at 1555 cm^{-1} for KGA-CNDs and at 1557 cm^{-1} for KGAMn-CNDs are observed, attributed to the presence of unsaturated C=C groups.[15,38,39] Additionally, intense absorption bands around 1393 cm^{-1} with a shoulder

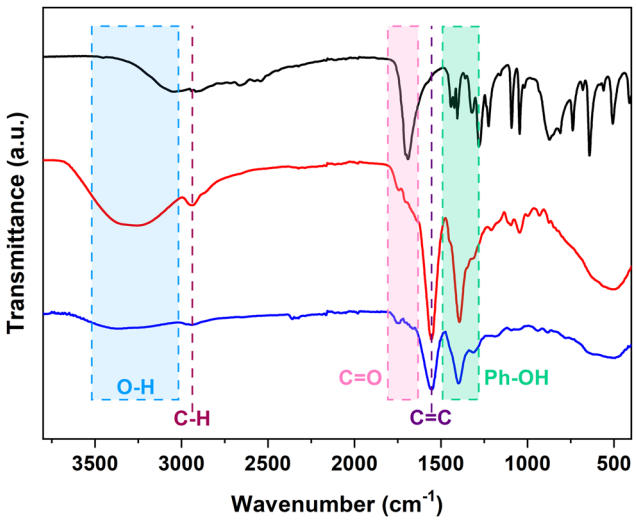

Fig. 2 ATR FT-IR spectra of pure KGA (black), KGA-CNDs (red) and KGAMn-CNDs (blue).

near 1313 cm^{-1} in KGA-CNDs (and similarly at 1397 cm^{-1} with the same shoulder in KGAMn-CNDs) are assigned to O–H bending vibrations typical of condensed aromatic structures.[40] These signals indicate the formation of sp^2-hybridized carbon networks occurring during the hydrothermal carbonization of KGA. Moreover, weaker bands at 1743 cm^{-1} (KGA-CNDs) and 1748 cm^{-1} (KGAMn-CNDs) suggest the presence of cyclic and ester carbonyl groups. Moreover, bands appearing as a flattened shoulder in the 1690–1720 cm^{-1} range, associated with C=O stretching vibrations of carboxylic groups, are present in both Mn-doped and non-doped CNDs. These spectral features confirm a moderate functionalization of CNDs with hydroxyl, carbonyl, and carboxylic groups. The key features of KGA-CNDs are also observed in KGAMn-CNDs, although slightly shifted by 3–4 cm^{-1} toward higher wavenumbers. Furthermore, the broad peak around 3300 cm^{-1} are attributed to O–H stretching vibrations of hydroxyl groups, while the small peak near 2900 cm^{-1} corresponds to C–H stretching vibrations.

XPS analysis. The transformation of the chemical structure from KGA into CNDs was assessed by XPS. After the carbonization process, the XPS spectra (Table 1) indicate an increase in carbon content and a corresponding decrease in oxygen content. This modification aligns with the anticipated loss of oxygenated surface functions during thermal processing. High-resolution XPS spectra were analysed through peak

Table 1 Surface elemental composition (at%) of the studied samples determined by XPS analysis

Surface Composition (at%)	KGA	KGA-CND	KGAMn-CND
Carbon	57.09	68.6	64.2
Oxygen	42.91	31.4	30.0
Manganesse	—	—	5.8

deconvolution to explain the evolution of surface chemistry across the samples, facilitating the identification of changes in specific functional groups and bonding environments (Fig. 3). The C 1s spectrum in the KGA precursor (Fig. 3a) exhibited a predominance of aliphatic carbon (C–C, 42.8%) and carbonyl species (C═O, 36.1%), consistent with the characteristics of an oxygen-rich organic acid, with smaller contributions from hydroxyl/ether (11.5%) and carboxylate groups (9.6%) (Table S1). The carbonization process resulted in the formation of sp^2-hybridized carbon (C═C, 46.0%) within the KGA-CNDs, indicating the development of a graphitic-like structure (Fig. 3b). C–O and O–C═O oxygen-containing surface groups were partially retained from the precursor but also formed during the synthesis process (Table S1). The KGAMn-CNDs (Fig. 3c) exhibited a comparable sp^2 carbon character (C═C, 43.5%) to the undoped samples, accompanied by a notable decrease in carboxylate groups (5.3%) and a concomitant increase in carbonyl functionalities (17.6%). This compositional shift indicates that manganese doping alters the surface chemistry of the CNDs. The O 1s spectrum further supports this observation, displaying a new peak at 531.6 eV, which is assigned to Mn–O or Mn–O–C bonding (Fig. 3f). This finding suggests active coordination of manganese ions to surface oxygen-containing groups, potentially modifying the electronic structure through the introduction of trap states.[41] These surface chemistry changes are likely to influence the photophysical behavior of the manganese-doped CNDs, affecting both of their emission wavelength and quantum yield.

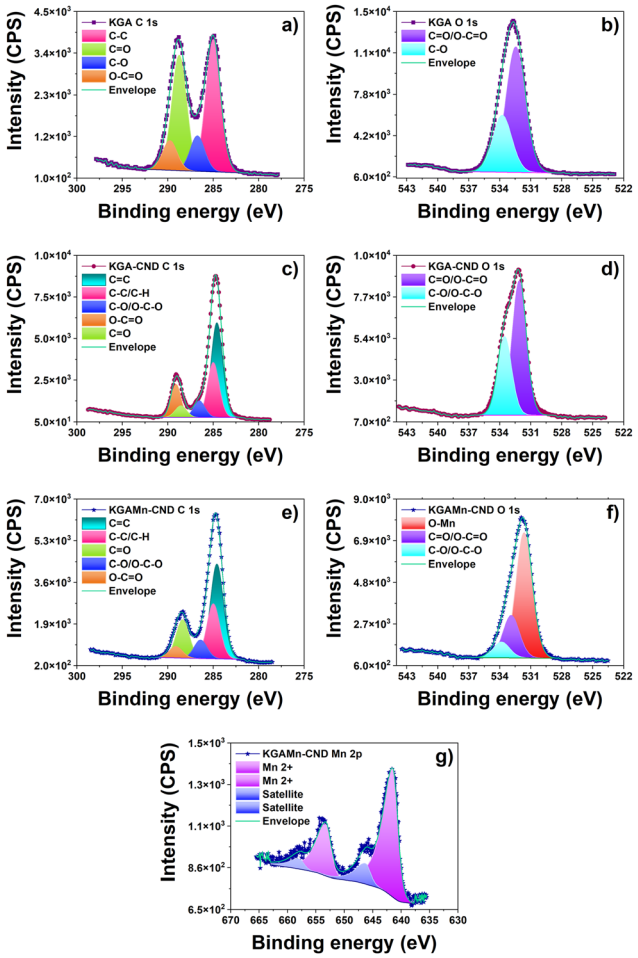

Fig. 3 High-resolution XPS spectra of pure KGA: (a) C 1s and (b) O 1s; KGA-CNDs: (c) C 1s and (d) O 1s; and KGAMn-CNDs: (e) C 1s, (f) O 1s, (g) Mn^{2+} 2p.

The O 1s spectra confirmed both the structural changes and the coordination of metal ions observed in the CNDs systems. KGA precursor has shown that oxygen signal exists through carbonyl and carboxyl groups (68.7%), along with hydroxyl (–OH) and ether (O–C–O) functionalities (31.3%) (Fig. 3d and Table S2). In the KGA-CNDs, the distribution is similar, with oxygen primarily associated with C═O and O–C═O groups (63.1%), indicating an incomplete retention of the precursor's oxygen functionalities post-carbonization (Fig. 3e and Table S2). However, in KGAMn-CNDs, an important change is observed, with a decrease in the C═O/O–C═O oxygen bound proportion (23.2%) (Fig. 3f and Table S2). At the same time, a new component associated with Mn–O bonding becomes the predominant signal at 68.1%. The observed redistribution aligns with the coordination of Mn^{2+} ions with surface-bound carboxyl or carbonyl groups.[26,41] The Mn 2p high-resolution spectra (Fig. 3g) confirmed the presence of the Mn–O bonding, proving the manganese incorporation. The evidence from O 1s and Mn 2p spectra demonstrates that manganese ions are chemically coordinated to the surface rather than adsorbed, which may influence the surface electronic structure.[12,15,26,42,43] Such coordination may introduce additional mid-gap states, affect carrier recombination dynamics, or passivate non-radiative sites, all of which are important in tuning the optical and electronic properties of the doped CNDs.[42,43]

The high-resolution Mn 2p XPS spectrum of the KGAMn-CNDs (Fig. 3g) reveals the presence of Mn^{2+} oxidation states. The high-spin Mn^{2+} was identified through the Mn $2p_{3/2}$ peak at 641.5 eV and a strong satellite at 646.3 eV.[15,26] The Mn and O spectra gave evidence that manganese is chemically bonded within the CNDs structure. This coordination is expected to influence the optical properties of the obtained materials, which may alter their fluorescence emission, lifetime, and QY.

EDX elemental mapping. EDX mapping for elemental analysis revealed a uniform distribution of carbon and oxygen atoms, showing no discontinuities that would suggest inhomogeneity in the examined samples (Fig. 4). Additionally, the elemental maps in Fig. 4d–g confirm a homogeneous distribution of manganese within the KGAMn-CNDs sample, with no evidence of aggregation or phase segregation.

Fig. 4a shows that the atomic ratio of carbon to oxygen in KGA-CNDs is 5.6 : 1, signifiantly higher than the theoretical C : O ratio of 1.66 : 1 for pure KGA. TThis increase indicates carbon enrichment resulting from the hydrothermal treatment of the KGA precursor. By comparison, the KGAMn-CNDs exhibit an atomic ratio of C : O : Mn equal to 2.76 : 1 : 0.24

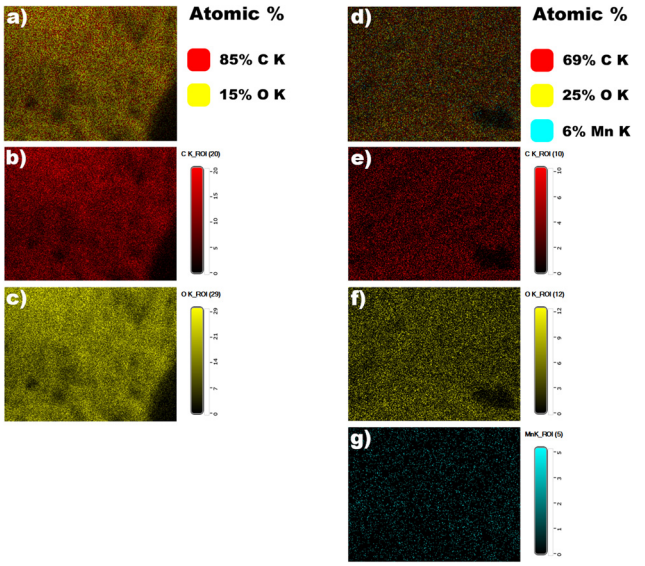

Fig. 4 EDX elemental mapping of KGA-CNDs (a) and KGAMn-CNDs (d), illustrating the spatial distribution of carbon and oxygen in KGA-CNDs (b and c) and KGAMn-CNDs (e and f), as well as the presence of manganese in KGAMn-CNDs (g).

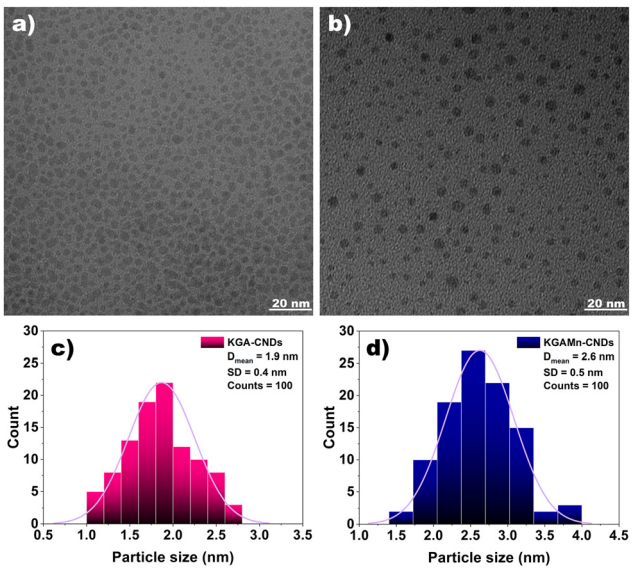

Fig. 5 TEM images of KGA-CNDs (a), KGAMn-CNDs (b) with corresponding particle size distribution histograms: KGA-CNDs (c), KGAMn-CNDs (d).

(Fig. 4d), reflecting a modest rise in oxygen content accompanying manganese doping, which is less evident in the XPS spectral analysis. Nevertheless, the manganese content in KGAMn-CNDs as determined by EDX (6.04 at%) closely aligns with the value obtained from XPS measurements (5.8 at%, as shown in Table 1).

Size and morphology studies by TEM. Transmission electron microscopy (TEM) analysis revealed that the synthesized CNDs are ultra-small, uniformly distributed nanoparticles with no significant agglomeration observed (Fig. 5). The KGA-CNDs (Fig. 5a) exhibited relatively low image contrast, which is attributed to their composition of light elements such as carbon and oxygen that possess low electron density. In contrast, the KGAMn-CNDs (Fig. 5b) displayed enhanced contrast and resolution, reflecting the higher electron density introduced by manganese doping. Both samples possessed a quasi-spherical morphology; however, the manganese-doped CNDs showed greater variability in particle size compared to the undoped CNDs. Specifically, KGA-CNDs had an average diameter of 1.9 nm with a narrow size distribution (Fig. 5c), whereas KGAMn-CNDs exhibited a broader size range from 2 to 3.3 nm and an average diameter of approximately 2.6 nm (Fig. 5d). The larger average diameter of KGAMn-CNDs relative to KGA-CNDs, coupled with the enhanced contrast in the manganese-doped samples, indirectly indicates the successful incorporation of manganese into the CNDs.

XRD analysis of CNDs. The XRD pattern of KGA-CNDs (Fig. 6, pink) presents a broad peak at 2θ angle around 20°, which corresponds to an interplanar d-spacing (d) value of about 4.44 Å (Table S2). This feature is commonly observed in CNDs patterns. The literature indicates that the peak's broadness is characteristic of the nanoscale dimensions and amorphous nature of the CNDs sample.[44] The measured 2θ angle and d-spacing values suggests a (002) diffraction plane of the graphitic carbon structure with an elevated degree of functionalization.[45] This pattern remains similar to that found in graphene oxide, which typically presents a 2θ angle around 26.7° and a d-spacing around 3.4 Å.[46] The observed shift indicates a possible increase in interlayer distance, often attributed to the incorporation of oxygen functional groups, water molecules, or other structural modifications.[46,47] Also, a diffraction peak at 2$\theta \approx 37.3°$ (Table S2) corresponding to a d-spacing of 2.40 Å is significantly smaller than the typical π–π stacking distance (the optimal d-spacing is considered ~3.4 Å),[46] suggesting the presence of specific crystallographic constraints.[48] This stacking behaviour aligns with previous studies

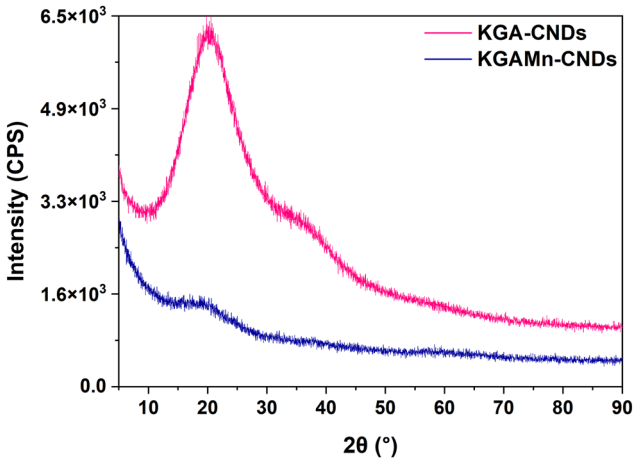

Fig. 6 The diffractogram of KGA-CNDs (pink) and KGAMn-CNDs (blue).

on turbostratic carbon, which explain interlayer distance variations as a result of functionalization.[47,49]

The KGAMn-CNDs diffractogram (Fig. 6, blue) exhibits a broad peak around 18.49° and a very small peak at 36°, indicating, as mentioned before, the presence of an amorphous phase of nanodimensional morphology.[50] The broader peak at $2\theta \approx 18.49°$ (Table S2), corresponding to an interplanar spacing (d) of 4.80 Å is typical for stacking of graphitic structure with a high degree of functionalization.[46] However, compared with KGA-CNDs, this peak suggests that the doping with manganese increases the disorder of the aromatic stacking, which serves as evidence that manganese successfully doped the CNDs. The other very small and broad peak at $2\theta \approx 36.56°$, corresponding to an interplanar spacing of 2.46 Å, is of low structural significance and does not strongly influence the overall structural features.

ESR analysis of KGAMn-CNDs. The presence of manganese in KGAMn-CNDs was also investigated and confirmed by ESR spectroscopy. The ESR spectrum of KGAMn-CNDs (Fig. 7) clearly exhibits the magnetic transitions characteristic of the divalent Mn^{2+} ions.[51] This spectrum is attributed to the manganese doped into the CNDs, as unbound ions were removed through the 72 hours dialysis step. ESR analysis of the dialysis water detected manganese in the early stages of dialysis, but no manganese was detectable after approximately 30 hours, confirming the efficient removal of free ions. The six magnetic transition lines from the spectrum indicate that Mn^{2+} ions are predominantly localized on the surface of KGAMn-CNDs.[52–54]

A calibration curve was generated from the ESR data by measuring the intensity of the third Mn^{2+} peak (marked with "*" in Fig. S1). By extrapolation from this calibration curve, a Mn^{2+} concentration of 0.6 mg mL^{-1} was determined in the 10 mg mL^{-1} KGAMn-CNDs solution. The ESR-determined concentrations enable the estimation of a Mn^{2+} ion content of approximately 6% in KGAMn-CNDs, a value that is consistent with the one obtained by EDX analysis (Fig. 4d) and closely matches the value measured by XPS (Table 1).

UV-Vis spectroscopy. The KGA-CNDs and KGAMn-CNDs exhibited comparable optical properties, featuring a pronounced absorption band in the 200–250 nm region. This band is attributed to high-energy n–σ* electronic transitions, typically associated with non-bonding electrons on oxygen-containing heteroatoms[55] (Fig. 8a). A secondary, less intense band in the 250–400 nm range is attributed to π–π* transitions of sp^2-hybridized aromatic structures,[56] along with n–π* transitions related to defect states in oxygen-containing functional groups.[57]

The optical bandgaps of the KGA precursor, KGA-CNDs, and KGAMn-CNDs were determined using Tauc plots,[58] based on UV-Vis absorption data (Fig. 8b and c). Plots were constructed for both direct $(\alpha h\nu)^2$ and indirect $(\alpha h\nu)^{1/2}$ allowed transitions to assess the nature of electronic transitions of the materials. This method provides insight into the electronic structure of the CNDs and enables comparison between the undoped and Mn-doped CNDs. The Tauc relation is defined by eqn (3).

$$(\alpha h\nu)^n = B(h\nu - E_g) \quad (3)$$

where: α – absorption coefficient (quantifying the amount of light absorbed by the material at a given photon energy); $h\nu$ – photon energy (h is Planck's constant and ν is the frequency of the incident light); B – constant that depends on the material and its electronic properties; E_g – material's optical band gap; n – type of electronic transition (n = 1/2 for direct transitions and n = 2 for indirect transitions).[58]

The extrapolated direct bandgap energies were determined to be 5.43 eV for KGA, 4.89 eV for KGA-CNDs, and 4.86 eV for KGAMn-CNDs (Fig. 8b). For indirect electronic transitions, the bandgap values were estimated at 4.76 eV for KGA, 3.43 eV for

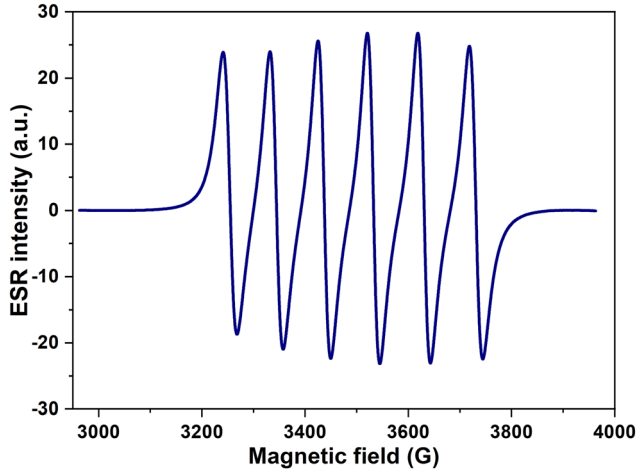

Fig. 7 ESR spectrum of KGAMn-CNDs (10 mg mL^{-1}) in water, recorded at room temperature.

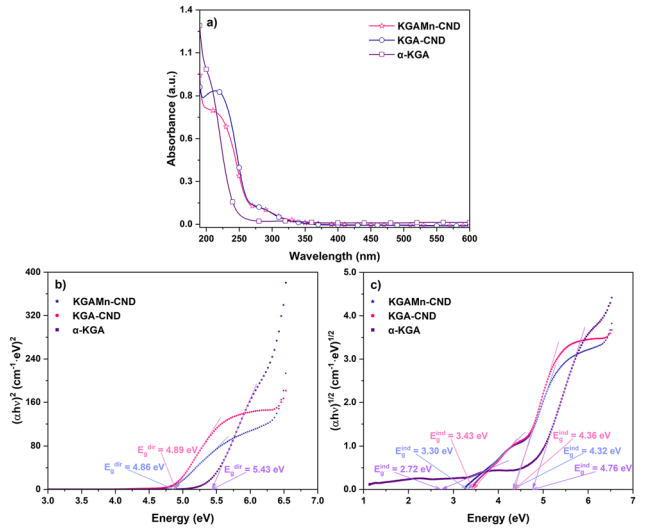

Fig. 8 UV-Vis absorption spectra (a) of pure KGA, KGA-CNDs and KGAMn-CNDs. Direct (b) and indirect (c) allowed transitions calculated from the UV-Vis data.

KGA-CNDs, and 3.30 eV for KGAMn-CNDs (Fig. 8c). The decrease in both direct and indirect bandgaps after carbonization is attributed to the development of sp^2-conjugated domains.[45]

Photoluminescence characteristics of CNDs. The PL analysis of KGA-CNDs and KGAMn-CNDs revealed a clear excitation-dependent behaviour, in which both the emission wavelength (λ_{em}) and fluorescence intensity vary with changes in the excitation wavelength (λ_{ex}), as illustrated in Fig. 9. Specifically, as λ_{ex} increases from 300 nm to 530 nm, the emission peak progressively red shifts from approximately 430 nm to 570 nm, reflecting the existence of multiple emissive surface states. However, throughout this excitation range, the fluorescence intensity of KGAMn-CNDs is significantly lower than that of the undoped CNDs, reflecting a quenching effect caused by Mn^{2+} ions. This quenching is likely due to non-radiative processes introduced by manganese doping that decrease the emission efficiency. Nevertheless, despite the reduced intensity, the KGAMn-CNDs retain a similar excitation peak region, implying that manganese incorporation affects emission strength but does not fundamentally change the excitation–emission relationship.

The emissive behaviour described above shows that the highest PL emission intensity occurs when the n–π* absorption band is excited, whereas excitation at the higher end of the π–π* band results in moderate PL intensity. The close similarity in the shape and position of the PL emission bands for both KGA-CNDs and KGAMn-CNDs indicates they share similar emission mechanisms and electronic structures. However, despite the nearly identical emission spectra, the PL intensity of the KGAMn-CNDs is about half that of the KGA-CNDs. This reduction in fluorescence intensity is due to a quenching effect from the Mn^{2+} ions, which lowers emission strength without causing a noticeable shift in the emission wavelength.

The excitation spectra of both samples, as presented in Fig. S3, showed a dominant excitation peak around 415 nm, indicating similar electronic transition pathways. The similarity in their spectral profiles indicates that manganese doping does not substantially affect the fundamental excitation characteristics of the CNDs. Moreover, the synthesized CNDs demonstrated large Stokes shifts (Fig. S3c), which can be attributed to emission originating from surface states associated with carboxyl functional groups.[59]

Influence of manganese ions. The effect of Mn^{2+} ions on KGA-CNDs was studied by adding varying amounts of $MnCl_2$ to a nanoparticle suspension, while keeping the nanoparticle concentration constant at 5 mg mL^{-1}. The $MnCl_2$ concentration ranged from 0 to 10 mg mL^{-1}, corresponding to 0–2.77 mg mL^{-1} of Mn^{2+} (up to a maximum manganese concentration of 50 mM) (Fig. 10). PL emission spectra were recorded under 420 nm excitation, showing that increasing $MnCl_2$ concentration did not cause any noticeable shift in the fluorescence bands (Fig. 10a). This agrees with earlier observations comparing the PL emission of KGA-CNDs and KGAMn-CNDs. Unlike the significant PL quenching seen when manganese is incorporated during synthesis (KGAMn-CNDs), the PL intensity of KGA-CNDs remained fairly stable with increasing free Mn^{2+} ions in solution, decreasing by only about 12% at the highest Mn^{2+} concentration tested (Fig. 10b). In contrast, KGAMn-CNDs showed roughly a 50% reduction in PL intensity relative to undoped KGA-CNDs (Fig. 9). These results suggest that the changes in optical properties of KGAMn-CNDs arise from manganese being integrated into the carbon nanodot structure during synthesis, rather than from simple interactions with residual $MnCl_2$. This highlights the direct role of manganese incorporation in modifying the photoluminescence behaviour.

Influence of saline environment and proteins on PL intensity. The analysis of PL behaviour in saline solutions shows that the PL intensity of the CNDs remains largely stable as the concentration of NaCl increases up to 10 mg mL^{-1} (Fig. 11a). This indicates that sodium and chloride ions do not cause any quenching effect. Furthermore, since chloride ions do not quench fluorescence, the reduction in PL intensity observed in KGAMn-CNDs relative to KGA-CNDs can be attributed to manganese incorporation within the CNDs structure rather than contamination from chloride ions introduced by$MnCl_2$. The stable PL emission of CNDs in the presence of NaCl is especially beneficial for biomedical applications, where Na^+ and Cl^- are abundant.

Similarly, the effect of proteins on PL intensity was examined using bovine serum albumin (BSA), a commonly employed model protein due to its 77% sequence similarity

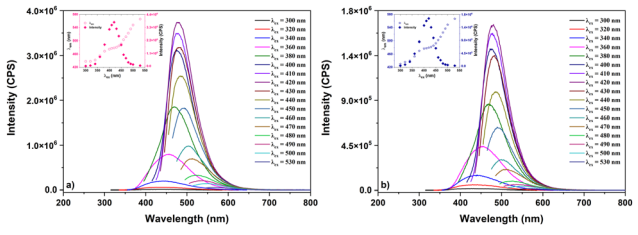

Fig. 9 Photoluminescence emission spectra of KGA-CNDs (a) and KGAMn-CNDs (b) recorded at different excitation wavelengths. Insets: correlation between emission wavelength (λ_{em}), excitation wavelength (λ_{ex}), and PL intensity.

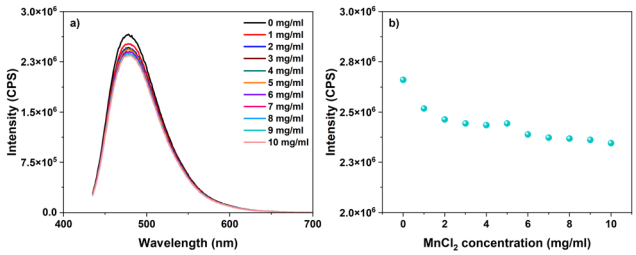

Fig. 10 PL spectra of KGA-CNDs (a) and the variation of PL intensity (b) at the excitation wavelength of 420 nm as a function of MnCl2 concentration.

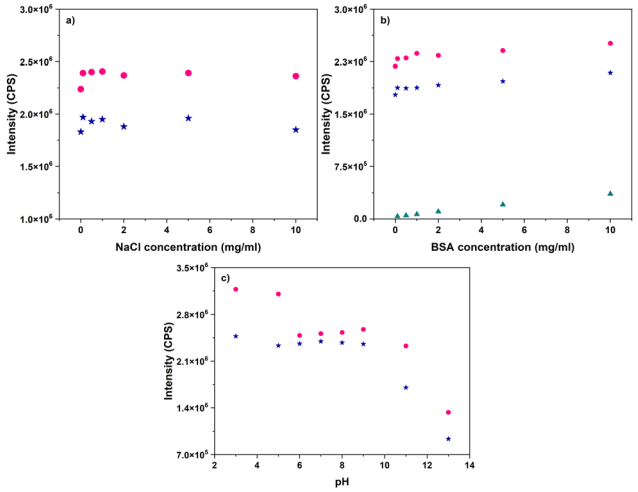

Fig. 11 Effect of NaCl (a), BSA (b) and pH (c) on the PL intensity of KGA-CNDs (circles) and KGAMn-CNDs (stars) at an excitation wavelength of 420 nm. In (c), the green triangles represent the PL intensity of BSA in the absence of CNDs (measured in PBS at pH 7).

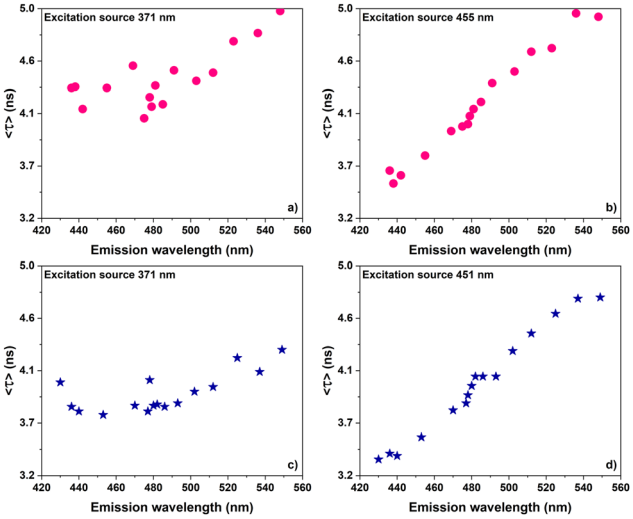

Fig. 12 Excited-state lifetime as a function of emission wavelength for KGA-CNDs using excitation wavelengths of (a) 371 nm and (b) 455 nm, and for KGAMn-CNDs using excitation wavelengths of (c) 371 nm and (d) 455 nm.

with human serum albumin (Fig. 11b).[60] Across the tested BSA concentration range (0–10 mg mL^{-1}), no significant alteration in CNDs' photoluminescence intensity was detected, indicating that proteins do not substantially influence their optical properties. Moreover, as depicted in Fig. 11b (green triangles), BSA exhibits only weak PL emission under 420 nm excitation, confirming that it does not interfere with the PL signals from the CNDs within the studied concentration range.

Influence of pH on PL intensity. The influence of pH on the PL intensity of the CNDs was examined in PBS across a pH range of 3 to 13. As shown in Fig. 11c (circles), the PL intensity of KGA-CNDs remains fairly stable from pH 3 to 5, then experiences a sharp decline at pH 6, and subsequently stays constant between pH 6 and 9. In contrast, the PL intensity of KGAMn-CNDs exhibits only a modest decrease between pH 3 and 6, followed by a similar plateau from pH 6 to 9 (Fig. 11c, stars). These observations are consistent with the work of Huanhuan Fan *et al.*,[61] who reported that acidic conditions generally enhance the emissive properties of such nanodots.

Lifetime, quantum yield and transient absorption measurements. Doping carbon nanodots (CNDs) with manganese ions (Mn^{2+}) is known to influence the surface electronic structure by altering surface states or introducing defects, which consequently affect excited-state relaxation dynamics. Fluorescence decay analyses of KGA-CNDs and KGAMn-CNDs, conducted under excitation wavelengths of 371 nm and 455 nm (Fig. 12a–d and Fig. S4–S7), reveal distinct decay behaviours fitted with a multiexponential function comprising two fast components (~0.5–3.5 ns) and one longer component (4–8.5 ns) (Table S3).

At 455 nm excitation, the excited-state lifetimes for KGA-CNDs range from 3.5 to 4.93 ns, while KGAMn-CNDs display slightly shorter lifetimes of 3.34 to 4.73 ns (Table S3). Lifetimes increase gradually with longer emission wavelengths, consistent with slower radiative recombination associated primarily with surface states rather than core transitions. The comparable lifetime ranges observed in both doped and undoped CNDs indicate that the interaction between Mn^{2+} ions and the CND surface is predominantly static. This suggests that Mn^{2+} ions are primarily anchored on or near the nanoparticle surface, rather than participating in dynamic excited-state interactions[62,63] (a conclusion supported also by ESR analysis). When measured at maximum PL emission (around 479–480 nm emission wavelength) under 455 nm excitation, KGA-CNDs and KGAMn-CNDs exhibit comparable lifetimes of 4.08 ns and 3.97 ns respectively, differing by less than 1 ns. Similar trends are observed at 371 nm excitation, highlighting consistent behaviour across excitation conditions (Table S3 and Fig. 12a, c).

Absolute quantum yields, measured over the range of excitation wavelengths (Fig. 13), reflect the typical excitation-dependent behavior common in CNDs. The QYs increase from the ultraviolet region and reach a maximum between 420 and 460 nm excitation. At 420 nm excitation, QYs are 16.72% for KGA-CNDs and 15.81% for KGAMn-CNDs. At 440 nm excitation, QYs increase to 20.26% and 16.66% respectively, further indicating the presence of multiple emissive states, especially those linked to surface defects.

The QY values obtained using KGA as a single precursor are in line with literature reports for single-precursor CND syntheses. For instance, folic acid-derived CNDs (which contain nitrogen dopants known to enhance radiative recombination) show QYs near 10% and have demonstrated usefulness in cell line staining.[31] However, folic acid contains nitrogen atoms, which inherently function as dopants that enhance radiative recombination processes.[64] In contrast, single-precursor CNDs lacking typical heteroatom dopants (N, S, B, P) remain less explored but generally exhibit QYs up to 20%.[65] Within this

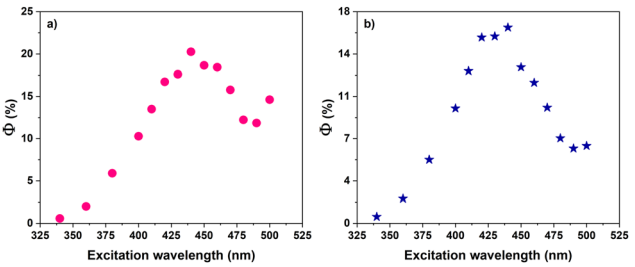

Fig. 13 Graphical representation of the absolute quantum yield as a function of excitation wavelength for KGA-CNDs (a) and KGAMn-CNDs (b).

context, the QYs of approximately 16%-20% obtained here for KGAMn-CNDs and KGA-CNDs underscore the effectiveness of KGA as a precursor for synthesizing highly emissive carbon nanodots.

The decay rates presented in Table S3 were calculated from the nanosecond fluorescence lifetime measurements and quantum yield (QY) values of KGA-CNDs and KGAMn-CNDs samples, using eqn (4)–(6):[62,66]

$$\frac{1}{\langle\tau\rangle} = k = k_r + k_{nr} \quad (4)$$

$$k_r = \frac{\Phi}{\langle\tau\rangle} \quad (5)$$

$$k_{nr} = \frac{1-\Phi}{\langle\tau\rangle} \quad (6)$$

where: k – total fluorescence decay rate constant (s^{-1}); k_r – radiative decay rate constant (s^{-1}); k_{nr} – non-radiative decay rate constants (s^{-1}); τ – average fluorescence lifetime (ns); Φ – quantum yield (QY).

Both radiative and non-radiative decay rates varied depending on the excitation wavelength and corresponding QY, as summarized in Table S3. Notably, the non-radiative decay constants were higher than the radiative ones in both KGA-CNDs and KGAMn-CNDs, indicating that non-radiative deactivation is the dominant relaxation pathway. This behaviour is attributed to the presence of excited states with n–π* character, which are known to facilitate ultra-fast non-radiative de-excitation channels upon photon absorption. These low-lying transitions are generally linked to lone electron pairs on surface oxygen atoms, which promote energy loss *via* non-emissive channels. The radiative decay constants followed an excitation-dependent trend, increasing with QY. Compared to KGA-CNDs, KGAMn-CNDs exhibited slightly decreased radiative decay rates alongside increased non-radiative decay rates, suggesting that manganese doping introduces additional non-radiative pathways, likely through trap states or modified surface coordination (as supported by XPS analysis). Under 455 nm excitation, both samples displayed slightly shorter average lifetimes and faster total decay rates, suggesting preferential excitation of lower-energy emissive states. Together, these findings support the hypothesis that manganese incorporation subtly modifies the surface electronic structure.

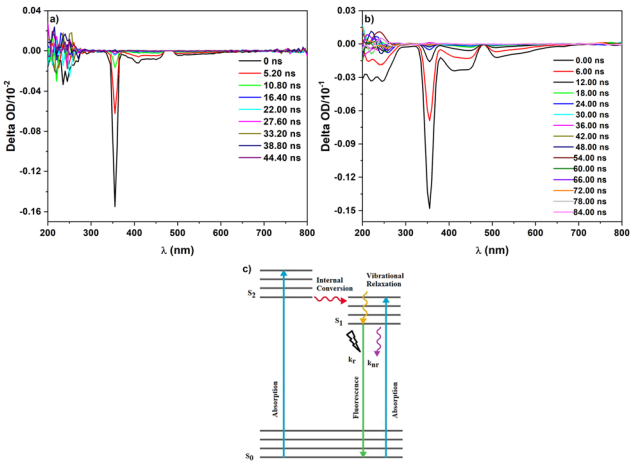

Fig. 14 Transitions absorption spectra of KGA-CNDs (a) and KGAMn-CNDs (b) in water, along with an illustration of the energy diagram (c).

As illustrated in Fig. 14, nanosecond transient absorption (TA) spectroscopy was employed to investigate the excited-state dynamics and the participation of higher-lying electronic states (Sn > 1) in both KGA-CNDs and KGAMn-CNDs. The TA map for KGA-CNDs dispersed in water (Fig. 14a) revealed characteristic photophysical features, including ground-state bleaching (GSB) bands at 245 and 255 nm and excited-state absorption (ESA) signals at 210, 230, and 240 nm, indicative of multiple excited states. At longer wavelengths, stimulated emission (SE) bands appeared at 405 and 445 nm, with additional SE features at 510 and 570 nm. The TA map for KGAMn-CNDs (Fig. 14b) exhibited similar photophysical characteristics, with GSB bands at 220 and 245 nm, ESA bands at 210, 215, and 235 nm, and SE bands at 410, 445, 510, and 570 nm. Together, these observations confirm the presence of multiple excited states and complex relaxation pathways within both CND systems (Fig. 14c).

Fluorescent and MR imaging properties of CNDs

Fluorescence imaging. Fluorescence imaging of the synthesized KGA-CNDs and KGAMn-CNDs was carried out following the procedure described in the Materials and Methods section. The resulting fluorescence images, shown in Fig. 15, correspond to samples at specified concentrations after the first (Fig. 15a) and tenth (Fig. 15b) consecutive scans. As illustrated in Fig. 15, the PL intensity within each region of interest (ROI) was quantified, revealing a clear concentration-dependent decrease in PL intensity with decreasing nanoparticle concentration. Furthermore, only a minimal decline in PL intensity was observed after ten sequential scans, demonstrating excellent photostability. This property is particularly important for *in vivo* imaging applications, where repeated scanning over prolonged periods is necessary to monitor the biodistribution and pharmacokinetics of imaging agents.[67] These findings suggest that both KGA-CNDs and KGAMn-CNDs are promising candidates for longitudinal fluorescence imaging in biological systems.

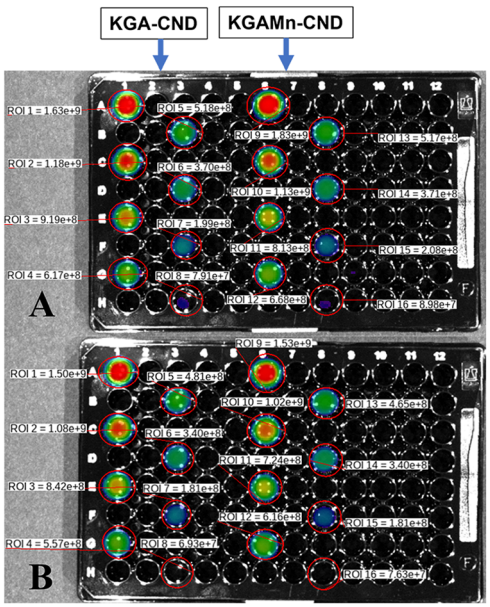

Fig. 15 Fluorescence imaging of KGA-CNDs and KGAMn-CNDs after first (a) and 10th scan (b). The concentration of both compounds decrease from top to bottom, while the colour of the wells changes from red-orange, representing the highest intensity fluorescence, to green and blue, for weak fluorescence.

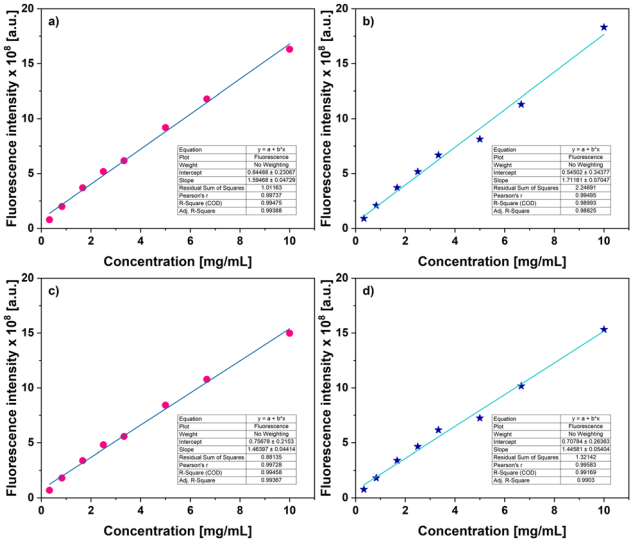

Fig. 16 Graphs of linear dependence of fluorescence intensity on concentration of compounds KGA-CNDs (a and c) and KGAMn-CNDs (b and d). The upper line in the figure presents the graphs of the two compounds at the first scan (a and b), and the bottom line presents the graphs obtained after the 10th scan (c and d). The slopes of the lines slightly decrease from 1.59 and 1.71 to 1.46 and 1.44 for KGA-CND and KGAMn-CND, respectively.

Additionally, plotting PL intensity as a function of CND concentration yielded a strong linear relationship over a wide concentration range (0.33 to 10 mg mL^{-1}), with coefficients of determination (R^2) exceeding 0.98, as depicted in Fig. 16. The slopes of the calibration curves were 1.59 and 1.71 for KGA-CNDs and KGAMn-CNDs, respectively (Fig. 16a and b), reflecting good contrast and consistency with values reported in the literature.[68,69] After ten scans, the slopes decreased slightly to around 1.4 for both compounds (Fig. 16c and d), further supporting the high photostability of these nanodots under prolonged imaging conditions.[70]

MR imaging. MRI images of KGAMn-CNDs dispersed in 1% agarose at varying concentrations, acquired using the parameters described in the Materials and Methods section, are shown in Fig. 17. As illustrated, the T_1-weighted GRE sequence produced the greatest contrast enhancement at flip angles (FA) of 60° and 70° among those tested. The classical T_1-weighted GRE acquisitions, characterized with a positive contrast, have presented maximum intensity at FA = 60–70°, being close to the calculated Ernst angle, which represents the optimal flip angle for a GRE acquisitions and depends on the estimated T_1 value and on the repetition time (TR).[71] The Ernst angle range was calculated between 74.15161876° and 89.89260501°.[72] This optimal FA range provided the best compromise between T_1 shortening and signal-to-noise ratio, resulting in a strong positive contrast where the images became progressively brighter with increasing manganese concentration. In contrast, classical T_2-weighted sequences generate negative contrast by shortening T_2, causing signal loss and darker images in regions containing the contrast agent. In the T_2-weighted

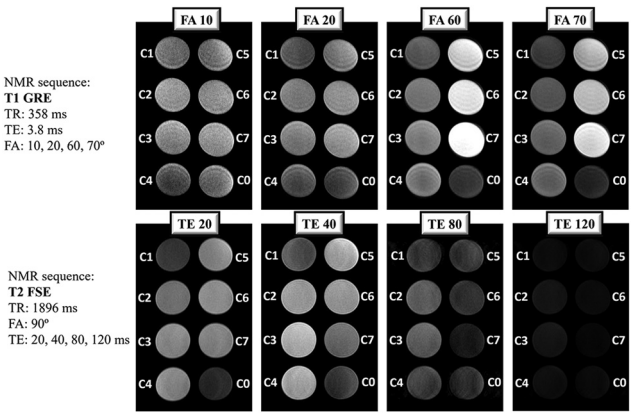

Fig. 17 MR images of KGAMn-CND dispersed in 1% agarose at serial concentrations, ranging from 0.027 to 0.33 mM, using as acquisition sequences T_1 GRE (upper line) and T_2 FSE (bottom line). In both T_1 and T_2 sequences there was one variable parameter, FA and TE, respectively.

fast spin echo (FSE) experiments, a clear dependence on echo time (TE) was observed. At a short TE of 20 ms, areas with higher manganese concentration showed increased signal intensity, indicating that T_2 decay was insufficient to produce significant contrast at this echo time. At TE = 40 ms, transitional behaviour was observed, characterized by a reduction in signal contrast between samples of varying concentrations due to pronounced free induction decay effects. By TE = 80 ms, significant signal attenuation occurred, with the signal amplitude decreasing clearly in proportion to concentration, reflecting the dominant influence of T_2* shortening typical of T_2-

weighted sequences. These findings indicate that, for both T_1- and T_2-weighted imaging sequences, contrast can be optimized through careful selection of imaging parameters, thereby improving the visibility and differentiation of concentration-dependent signal changes.[73]

Relaxation times T_1 and T_2 were determined for each manganese concentration in the KGAMn-CND samples, and the corresponding relaxation rates, $r_1 = 1/T_1$ and $r_2 = 1/T_2$, were subsequently calculated and plotted as functions of molar concentration. Linear regression of the data (Fig. 18) yielded relaxivity values of 5.46 s^{-1} mM^{-1} for r_1 and 46.83 s^{-1} mM^{-1} for r_2, as summarized in the inset table of Fig. 18. Generally, higher relaxivity values indicate greater efficacy as MRI contrast agents, due to enhanced modulation of proton relaxation times.[74] The resulting r_2/r_1 ratio of 8.4 signifies a predominantly T_2-weighted relaxation behaviour[75] in KGAMn-CNDs, consistent with the observed imaging contrast. Although these CNDs exhibit dual contrast properties at low echo times, the pronounced T_2 dominance highlights their potential as effective T_2 contrast agents, particularly at clinically relevant magnetic field strengths. Importantly, increasing manganese content improves T_2 relaxation efficiency *via* stronger dipolar interactions and susceptibility effects, which can cause negative contrast or signal attenuation in T_2-weighted images. The relaxivity ratio (r_2/r_1), which is based on the intrinsic properties of the agent, serves as an important parameter for classifying the agent's dominant contrast mechanism and for tracking transitions between T_1 and T_2 contrast behaviour.

For a rigorous evaluation of contrast agent efficacy, it is essential to compare relaxivities with those of clinically approved agents measured under the same magnetic field strength, as relaxivity values are intrinsic properties that depend strongly on field strength. Typically, r_1 decreases and r_2 increases with rising magnetic field strengths due to susceptibility effects and altered molecular correlation times.[23] Since most clinical data are reported at 1.5 T and 3 T, direct comparison with measurements at other fields can be challenging.[76] For instance, the commercial gadolinium-based agent Gadoterate[23] exhibits r_1 and r_2 relaxivities of 3.58 s^{-1} mM^{-1} and 21.6 s^{-1} mM^{-1}, respectively, measured at 0.5 T. Compared to these, the KGAMn-CNDs studied here at 1 T show considerably higher relaxivities (r_1 = 5.46 s^{-1} mM^{-1} and r_2 = 46.83 s^{-1} mM^{-1}), indicating competitive performance as dual-mode MRI contrast agents with strong capabilities in both T_1 and T_2-weighted imaging sequences.

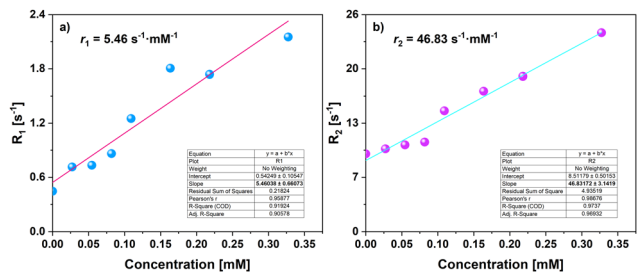

Fig. 18 Linear fitting of R_1 (a) and R_2 (b) as a function of molar concentration of Mn comprised in KGAMn-CND. The slopes of the lines represent the relaxivities r_1 and r_2, of 5.46 and 46.83 s^{-1} mM^{-1}, respectively.

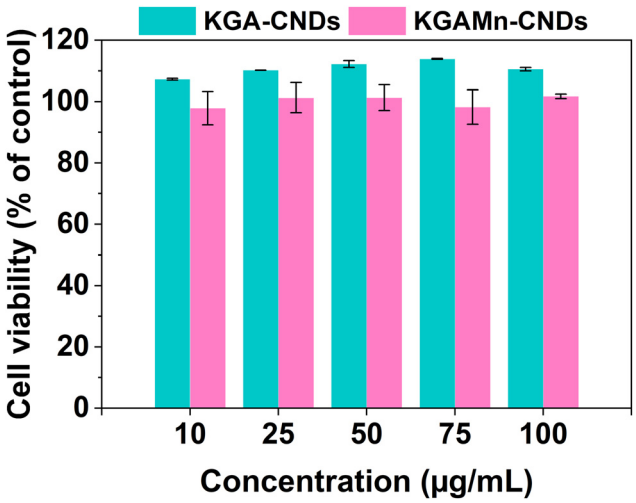

Fig. 19 Biocompatibility of CNDs on normal fibroblasts after 24 h.

***In vitro* biocompatibility.** The *in vitro* biocompatibility of CNDs was evaluated by incubating normal human gingival fibroblasts (HGF) with varying concentrations of CNDs (10, 25, 50, 75, and 100 μg mL^{-1}) for 24 hours. As shown in Fig. 19, the results demonstrate that the CNDs maintain good biocompatibility across all tested concentrations.

Conclusions

Biocompatible CNDs were synthesized through a one-step hydrothermal method using KGA, a biomolecule crucial for cellular metabolism, as the sole precursor. This study is thus significant for its initial evaluation of KGA as a viable carbon source for CND formation without the addition of other precursors or heteroatom dopants. Additionally, in this work was investigated the synthesis of manganese-doped CNDs, making use of the paramagnetic properties of manganese, which are beneficial for biomedical applications, especially as contrast agents in magnetic resonance imaging (MRI).

Both undoped and manganese-doped carbon nanodots demonstrated significant qua yields, despite the absence of additional heteroatom doping. The photoluminescence emission properties exhibited stability under physiological-like conditions, including saline solutions and media containing proteins, specifically using bovine serum albumin (BSA) as a model protein. Furthermore, PL intensity exhibited minimal variation across a physiologically relevant pH range of 5 to 9, which includes both normal and pathological conditions. Imaging experiments demonstrated their effectiveness as fluorescent contrast agents, exhibiting significant photostability under repeated irradiation, an essential characteristic for longitudinal imaging.

Manganese-doped CNDs serve effectively as MRI contrast agents owing to the paramagnetic properties of manganese. A

comparative analysis with other paramagnetic metal-based compounds showed that these manganese-doped CNDs demonstrate MRI contrast properties comparable to those of gadolinium-based agents, which are well-established in clinical applications.

Author contributions

Conceptualization, I. A. T. M., A. F, M. P.; formal analysis, A. C., I. A. T. M., T. P., A. F.; investigation, I. A. T. M., A. C., A. F., N. L. M., I. R. T, C. M. U., S. I. F., M. D., T. P.; methodology, I. A. T. M., A. C., A. F., N. L. M., C. M. U., S. I. F.; M. D.; supervision, A. F., M. P.; I. A. T. M. Validation, A. F., M. P.; visualization, I. A. T. M., A. F., M. P.; writing – original draft, A. F., I. A. T. M., A. C., C. M. U., M. P.; writing – review & editing, A. C., T. P., A. F., I. A. T. M., M. P.; all authors have read and agreed to the published version of the manuscript.

Conflicts of interest

There are no conflicts to declare.

Data availability

Data will be made available on request. The Supplementary Information file contains the calculation method for time-resolved fluorescence decay analysis, seven figures and three tables, as follows: Mn^{2+} calibration curve and characteristic ESR spectra of the Mn^{2+} ion at different concentrations (Fig. S1), zeta potential analysis of KGA-CNDs and KGAMn-CNDs (Fig. S2), excitation spectra of KGA-CNDs and KGAMn-CNDs and calculated Stokes shifts (Fig S3), fluorescence decay profiles of KGA-CNDs measured at an excitation wavelength of 371 nm at different emission wavelengths (Fig. S4), fluorescence decay profiles of KGAMn-CNDs measured at an excitation wavelength of 371 nm at different emission wavelengths (Fig. S5), fluorescence decay profiles of KGA-CNDs measured at an excitation wavelength of 455 nm at different emission wavelengths (Fig. S6), fluorescence decay profiles of KGAMn-CNDs measured at an excitation wavelength of 455 nm at different emission wavelengths (Fig. S7). relative distribution of surface groups (at., %) obtained after the deconvolution of the XPS data corresponding to the C1s, O1s and Mn 2p signals of the prepared samples (Table S1), interplanar spacing (d-spacing) values of KGA-CND and KGAMn-CND calculated from XRD diffraction patterns (Table S2), emission maxima, absolute PLQY, decay rate constants and lifetime of KGA-CND and KGAMn-CND in water (Table S3). See DOI: **https://doi.org/10.1039/d5nr03268g**.

Acknowledgements

The authors are thankful for the financial support from the grant of the Ministry of Research, Innovation and Digitization, project no. PNRR-III-C9-2022-I8-291, contract no. 760081/23.05.2023, within the National Recovery and Resilience Plan.

References

1 A. Kengelbach-Weigand, L. Lotz, R. Schmid, W. Lang, M. W. Beckmann, I. Hoffmann, R. E. Horch, S. P. Renner, R. Dittrich, A. M. Boos and T. Hildebrandt, *In Vivo*, 2019, **33**, 325–336.
2 P. Miao, K. Han, Y. Tang, B. Wang, T. Lin and W. Cheng, *Nanoscale*, 2015, **7**, 1586–1595.
3 S. Sawalha, S. Abdallah, A. Barham, H. Badawi, Z. Barham, A. Ghareeb, G. Misia, S. Collavini, A. Silvestri, M. Prato and M. Assali, *Nanoscale Adv.*, 2023, **5**, 5974–5982.
4 S. Sawalha, M. Assali, A. Yaseen, A. Ataya, L. Refai, R. Hamed, G. Misia, S. Collavini and A. Silvestri, *Mater. Today Sustain.*, 2024, **25**, 100697.
5 J. Zang, F. Jiao, J. Wei, Q. Lou, G. Zheng, C. Shen, Y. Deng, E. Soheyli, R. Sahraei, X. Yang, H. Zang, W. Zhou, W. Fan, S. Wang, L. Dong and C.-X. Shan, *Nanophotonics*, 2023, **12**, 4117–4126.
6 Y.-D. Xiao, R. Paudel, J. Liu, C. Ma, Z.-S. Zhang and S.-K. Zhou, *Int. J. Mol. Med.*, 2016, **38**, 1319–1326.
7 F. Martino, G. Amici, M. Rosner, C. Ronco and G. Novara, *J. Clin. Med.*, 2021, **10**, 271.
8 M. Botta, F. Carniato, D. Esteban-Gómez, C. Platas-Iglesias and L. Tei, *Future Med. Chem.*, 2019, **11**, 1461–1483.
9 C. Henoumont, M. Devreux and S. Laurent, *Molecules*, 2023, **28**, 7275.
10 E. A. Stepanidenko, A. A. Vedernikova, Z. F. Badrieva, E. A. Brui, S. O. Ondar, M. D. Miruschenko, O. V. Volina, A. V. Koroleva, E. V. Zhizhin and E. V. Ushakova, *Photonics*, 2023, **10**, 757.
11 M. Wang, H. Zhu, B. Liu, P. Hu, J. Pan and X. Niu, *ACS Appl. Mater. Interfaces*, 2022, **14**, 44762–44771.
12 Z. Zhang, Y. Xu, T. Zhu, Z. Sang, X. Guo, Y. Sun, Y. Hao and W. Wang, *Front. Bioeng. Biotechnol.*, 2023, **11**, 1153196.
13 H. Wang, D. Chu, M. Zhang, X. Huang, Y. Shi, Y. Zhao, H. Qu, D. Li, Z. Xu, L. Gao, X. Zhang and W. Wang, *Colloids Surf., B*, 2025, **246**, 114398.
14 H. Zhang, S. Yang and X. Zhou, *J. Mater. Sci.: Mater. Electron.*, 2022, **33**, 4170–4183.
15 S. Sun, Q. Guan, Y. Liu, B. Wei, Y. Yang and Z. Yu, *Chin. Chem. Lett.*, 2019, **30**, 1051–1054.
16 G. Liu, T. Li, Z. Li, Z. Li, C. Liu and Q. Wang, *J. Inorg. Organomet. Polym.*, 2024, **34**, 4642–4654.
17 E. A. Stepanidenko, A. A. Vedernikova, Z. F. Badrieva, E. A. Brui, S. O. Ondar, M. D. Miruschenko, O. V. Volina, A. V. Koroleva, E. V. Zhizhin and E. V. Ushakova, *Photonics*, 2023, **10**, 757.
18 N. Wu, M. Yang, U. Gaur, H. Xu, Y. Yao and D. Li, *Biomol. Ther.*, 2016, **24**, 1–8.
19 B. Gyanwali, Z. X. Lim, J. Soh, C. Lim, S. P. Guan, J. Goh, A. B. Maier and B. K. Kennedy, *Trends Endocrinol. Metab.*, 2022, **33**, 136–146.

20 S. Kostromin, A. Borodina, A. Podshivalov, D. Pankin, O. Zhigalina and S. Bronnikov, *Fullerenes, Nanotubes Carbon Nanostruct.*, 2023, **31**, 931–939.
21 R. Ludmerczki, S. Mura, C. M. Carbonaro, I. M. Mandity, M. Carraro, N. Senes, S. Garroni, G. Granozzi, L. Calvillo, S. Marras, L. Malfatti and P. Innocenzi, *Chem. – Eur. J.*, 2019, **25**, 11963–11974.
22 Y. Pan, J. Yang, Y. Fang, J. Zheng, R. Song and C. Yi, *J. Mater. Chem. B*, 2017, **5**, 92–101.
23 J. K. van Zandwijk, F. F. J. Simonis, F. G. Heslinga, E. I. S. Hofmeijer, R. H. Geelkerken and B. ten Haken, *PLoS One*, 2021, **16**, e0256252.
24 C. A. Schneider, W. S. Rasband and K. W. Eliceiri, *Nat. Methods*, 2012, **9**, 671–675.
25 B. Dragoi, C. M. Uritu, L. Agrigoroaie, D. Lutic, V. Hulea, G. Postole, A. Coroaba and E. Carasevici, *ACS Appl. Nano Mater.*, 2021, **4**, 2061–2075.
26 A. Tiron, C. S. Stan, G. Luta, C. M. Uritu, I.-C. Vacarean-Trandafir, G. D. Stanciu, A. Coroaba and C. E. Tiron, *Pharmaceutics*, 2021, **13**, 1982.
27 R. Ghiarasim, N. Simionescu, A. Coroaba, C. M. Uritu, N. L. Marangoci, S.-A. Ibanescu and M. Pinteala, *Int. J. Mol. Sci.*, 2021, **23**, 155.
28 H. Yusuff, S. Chatelin and J.-P. Dillenseger, *Radiography*, 2024, **30**, 1655–1668.
29 J. Yang, W. Chen, X. Liu, Y. Zhang and Y. Bai, *Mater. Res. Bull.*, 2017, **89**, 26–32.
30 M. Mihalache, O. Oprea, C. Guran and I. L. Ardelean, *Rev. Chim.*, 2017, **68**, 2209–2214.
31 W. Fawaz, J. Hasian and I. Alghoraibi, *Sci. Rep.*, 2023, **13**, 18641.
32 V. Nidhisha, G. Ritu, C. Anjali, T. P. Amrutha, K. K. Arunima, K. P. Vakayil and N. K. Renuka, *Nanoscale Adv.*, 2024, **6**, 1535–1547.
33 T. Pal, S. Mohiyuddin and G. Packirisamy, *ACS Omega*, 2018, **3**, 831–843.
34 M. Zulfajri, S. Dayalan, W.-Y. Li, C.-J. Chang, Y.-P. Chang and G. G. Huang, *Sensors*, 2019, **19**, 5008.
35 V. Vijayalakshmi, P. Dhanasekaran and J. Aarthi, *Appl. Phys. A*, 2022, **128**, 416.
36 FTIR Functional Group Database Table with Search – InstaNANO, **https://instanano.com/all/characterization/ftir/ftir-functional-group-search/**.
37 B. Fu, Q. Liu, M. Liu, X. Chen, H. Lin, Z. Zheng, J. Zhu, C. Dai, X. Dong and D.-P. Yang, *Chin. Chem. Lett.*, 2022, **33**, 4577–4582.
38 S. A. Al Kiey and H.-A. S. Tohamy, *J. Energy Storage*, 2024, **101**, 113758.
39 W. Gul and H. Alrobei, *Polymers*, 2021, **13**, 1818.
40 S. Xu, J. Zhao, Q. Yu, X. Qiu and K. Sasaki, *ACS Earth Space Chem.*, 2019, **3**, 2175–2189.
41 Z. Qin, J. Xu, Y. Cao, C. Liao and S. Shi, *Spectrochim. Acta, Part A*, 2025, **330**, 125688.
42 W. Xu, J. Zhang, Z. Yang, M. Zhao, H. Long, Q. Wu and F. Nian, *J. Mater. Sci.: Mater. Med.*, 2022, **33**, 16.
43 S. Sun, L. Zhao, D. Wu, H. Zhang, H. Lian, X. Zhao, A. Wu and L. Zeng, *ACS Appl. Bio Mater.*, 2021, **4**, 1969–1975.
44 H. Luo, L. Lari, H. Kim, S. Hérou, L. C. Tanase, V. K. Lazarov and M.-M. Titirici, *Nanoscale*, 2022, **14**, 910–918.
45 S. Supajaruwong, S. Porahong, A. Wibowo, Y.-S. Yu, M. J. Khan, P. Pongchaikul, P. Posoknistakul, N. Laosiripojana, K. C.-W. Wu and C. Sakdaronnarong, *Sci. Technol. Adv. Mater.*, 2023, **24**, 2260298.
46 A. N. Popova, *Coke Chem.*, 2017, **60**, 361–365.
47 R. Siburian, H. Sihotang, S. L. Raja, M. Supeno and C. Simanjuntak, *Orient. J. Chem.*, 2018, **34**, 182–187.
48 T. Ishida, M. Shibata, K. Fujii and M. Inoue, *Biochemistry*, 1983, **22**, 3571–3581.
49 Z. Q. Li, C. J. Lu, Z. P. Xia, Y. Zhou and Z. Luo, *Carbon*, 2007, **45**, 1686–1695.
50 D. D. Ferreyra, D. R. Sartori, E. S. D. Riega, H. B. Rodríguez and M. C. Gonzalez, *Carbon*, 2020, **167**, 230–243.
51 A. K. Kar, A. Acharya, G. C. Pradhan and A. C. Dash, *J. Chem. Sci.*, 2014, **126**, 547–559.
52 A. J. Yost, A. Pimachev, G. Rimal, J. Tang, Y. Dahnovsky and T. Chien, *Appl. Phys. Lett.*, 2017, **111**, 233101.
53 L. Turyanska, R. J. A. Hill, O. Makarovsky, F. Moro, A. N. Knott, O. J. Larkin, A. Patanè, A. Meaney, P. C. M. Christianen, M. W. Fay and R. J. Curry, *Nanoscale*, 2014, **6**, 8919–8925.
54 G. Counio, S. Esnouf, T. Gacoin and J.-P. Boilot, *J. Phys. Chem.*, 1996, **100**, 20021–20026.
55 W. A. Qureshi, B. Vivekanandan, J. A. Jayaprasath, D. Ali, S. Alarifi and K. Deshmukh, *J. Nanomater.*, 2021, **2021**, 9096838.
56 X. Li, L. Yan, J. Si, H. Xu and Y. Xu, *RSC Adv.*, 2019, **9**, 12732–12736.
57 M. M. Messina, S. D. Barrionuevo, M. E. Coustet, M. P. Kreuzer, F. D. Saccone, P. Cecilia dos Santos Claro and F. J. Ibañez, *ACS Appl. Nano Mater.*, 2021, **4**, 7309–7318.
58 J. Tauc and A. Menth, *J. Non-Cryst. Solids*, 1972, **8–10**, 569–585.
59 X. Zhang, Y. Liu, C.-H. Kuan, L. Tang, T. D. Krueger, S. Yeasmin, A. Ullah, C. Fang and L.-J. Cheng, *J. Mater. Chem. C*, 2023, **11**, 11476–11485.
60 N. Liu, M. Tang and J. Ding, *Chemosphere*, 2020, **245**, 125624.
61 H. Fan, G. Q. Xiang, Y. Wang, H. Zhang, K. Ning, J. Duan, L. He, X. Jiang and W. Zhao, *Spectrochim. Acta, Part A*, 2018, **205**, 221–226.
62 J. R. Lakowicz, *Principles of fluorescence spectroscopy*, Springer Science & Business Media, 2007.
63 T. T. Trang, T. T. H. Pham, N. V. Dang, P. T. Nga, M. V. Linh and X. H. Vu, *RSC Adv.*, 2024, **14**, 9538–9546.
64 M. B. Prado, N. T. Truong and A. K. Wanekaya, *Sens. Actuators Rep.*, 2023, **6**, 100165.
65 X. Zhai, P. Zhang, C. Liu, T. Bai, W. Li, L. Dai and W. Liu, *Chem. Commun.*, 2012, **48**, 7955–7957.
66 A. Coroaba, C. Al-Matarneh, T. Vasiliu, S.-A. Ibanescu, R. Zonda, I. Esanu, D.-L. Isac and M. Pinteala, *J. Mol. Liq.*, 2023, **374**, 121298.
67 J. Du, N. Xu, J. Fan, W. Sun and X. Peng, *Small*, 2019, **15**, 1805087.

68 T. Son, M. Kim, M. Choi, S. H. Nam, A. Yoo, H. Lee, E. H. Han, K. S. Hong and H. S. Park, *J. Nanobiotechnol.*, 2024, **22**, 347.
69 V. H. M. Doan, V. T. Nguyen, S. Mondal, T. M. T. Vo, C. D. Ly, D. D. Vu, G. Y. Ataklti, S. Park, J. Choi and J. Oh, *Sci. Rep.*, 2021, **11**, 15943.
70 W. U. Khan, L. Qin, W. U. Khan, S. U. Khan, M. M. Hussain, F. Ahmed, S. Kamal and P. Zhou, *ACS Appl. Nano Mater.*, 2023, **6**, 17838–17847.
71 D. Pan, A. H. Schmieder, S. A. Wickline and G. M. Lanza, *Tetrahedron*, 2011, **67**, 8431–8444.
72 O. W. Sørensen, *J. Magn. Reson. Open*, 2024, **19**, 100148.
73 H. Wilson, E. R. de Natale and M. Politis, in *Neuroimaging in Parkinson' s Disease and Related Disorders*, ed. M. Politis, H. Wilson and E. R. De Natale, Academic Press, 2023, pp. 21–52.
74 P. Caravan, J. J. Ellison, T. J. McMurry and R. B. Lauffer, *Chem. Rev.*, 1999, **99**, 2293–2352.
75 S. Caspani, R. Magalhães, J. P. Araújo and C. T. Sousa, *Materials*, 2020, **13**, 2586.
76 M. Rohrer, H. Bauer, J. Mintorovitch, M. Requardt and H.-J. Weinmann, *Invest. Radiol.*, 2005, **40**, 715.